

Nuclear level density of ^{128}Te from $(p, p'\gamma)$ scattering and complementary photonuclear data

P.-A. Söderström^{1,*}, A. Kuşoğlu^{1,2}, S. Aogaki¹,
 D. L. Balabanski¹, S.-R. Ban¹, R. Borcea³, M. Brezeanu¹,
 S. Calinescu³, C. Costache³, R. Corbu¹, M. Cuciuc¹, A. Dhal¹,
 I. Dinescu³, N. M. Florea³, T. Furuno⁴, A. Gavrilescu¹,
 A. Gupta⁵, Y. Honda⁴, J. Isaak⁵, N. C. Jerca¹, T. Kawabata⁴,
 V. Lelasseux¹, R. Lica³, C. Marin¹, C. Mihai³, S. Niculae¹,
 H. Pai¹, I. P. Pârlea¹, T. Petruse¹, A. Spataru¹, D. A. Testov¹,
 D. Tofan³, T. Tozar¹, A. Turturică³, G. V. Turturică¹,
 S. Ujeniuc³

¹ Extreme Light Infrastructure (ELI-NP), Horia Hulubei National Institute for R&D in Physics and Nuclear Engineering (IFIN-HH), Str. Reactorului No. 30, 077125 Bucharest-Măgurele, Romania

² Department of Physics, Faculty of Science, Istanbul University, Vezneciler/Fatih, 34134, Istanbul, Turkey

³ Department of Nuclear Physics, Horia Hulubei National Institute for R&D in Physics and Nuclear Engineering (IFIN-HH), Str. Reactorului No. 30, 077125 Bucharest-Măgurele, Romania

⁴ Department of Physics, Osaka University, Toyonaka, Osaka 560-0043, Japan

⁵ Institute for Nuclear Physics, Department of Physics, Technische Universität Darmstadt, Darmstadt 64289, Germany

E-mail: par.anders@eli-np.ro

17 January 2025

Abstract. We have extracted the nuclear level density of ^{128}Te from a $(p, p'\gamma)$ scattering experiment using the large-volume $\text{LaBr}_3\text{:Ce}$ and CeBr_3 detectors from ELI-NP at the 9 MV Tandem facilities at IFIN-HH. The decay data were normalised using photonuclear data, resulting in nuclear level densities without intrinsic model dependencies from the constant temperature or Fermi gas models. The measured nuclear level density follows closely between the expectations from these two models, but we observe a clear divergence from a microscopic model based on the Skyrme force.

1. Introduction

Statistical nuclear properties, like γ -ray strength functions (γSFs) and nuclear level densities (NLDs), are important measurable observables determining reaction rates for applications like nuclear reactor technologies and criticality, processing of spent nuclear

fuel, and nuclear astrophysics. These observables serve as input to the statistical model that describes the atomic nucleus at energies and temperatures where discrete states start to overlap due to their natural widths and can not be treated as separate energy states anymore. For a recent overview of the current experimental and theoretical status of NLDs and γ SF, see Reference [1]. Several different traditional methods exist for NLD measurements. These include the well-established Oslo method [2, 3, 4, 5], evaporation spectra of protons [6] or neutrons [7], or high-energy (p, p') scattering with magnetic spectrometers [8].

Another interesting opportunity for experimental studies of NLDs and γ SFs is the projected γ -ray beams at the Extreme Light Infrastructure – Nuclear Physics (ELI-NP) [9, 10, 11, 12, 13]. While charged-particle probes populate an extensive range of states, electromagnetic probes consisting of narrow bandwidth γ rays for photoexcitation and decay studies have high selectivity in excitation energy, spin, and parity of the ensemble of excited states. This has been explored in depth in pioneering work at the High-Intensity γ -ray Source (HI γ S) facility at the Triangle Universities Nuclear Laboratory (TUNL), Duke University, North Carolina, using the ($\vec{\gamma}, \gamma'\gamma''$) technique [14], meaning inelastic scattering of incoming polarised photons, $\vec{\gamma}$, with a two-step decay as γ' and γ'' to extract γ SFs directly. Due to the properties of the γ -ray beams, the γ SFs could be explicitly selected from electric dipole states and, also, for well-defined excitation energies providing the potential for a sensitive test of the Brink-Axel hypothesis [15, 16], that the γ SFs are independent of the excitation energy in the statistical region and only depend on the energy difference between the initial and final states.

While the γ -ray beams at ELI-NP are under implementation, a complementary scientific program has been started at the charged particle accelerator facilities at the Horia Hulubei Institute for Physics and Nuclear Engineering (IFIN-HH), in particular at the 9 MV Tandem accelerator facilities. In this programme, we utilise the instrumentation from ELI-NP, especially the ELI Gamma Above Neutron Threshold (ELIGANT) instruments [17, 18] and other setups in the existing ELI-NP and IFIN-HH infrastructure. One of the primary campaigns has been utilising the ROmanian array for SPectroscopy in HEavy ion REactions (ROSPHERE) [19] infrastructure and detection system in combination with the large-volume $\text{LaBr}_3\text{:Ce}$ and CeBr_3 detectors for a system dedicated to high-energy γ rays. This special version of ROSPHERE [20] has already succeeded in detailed studies of light nuclei and high-energy resonant states in medium-mass nuclei [21, 22, 23, 24, 25, 26, 27]. In addition to these experiments, an experiment dedicated to NLDs and γ SFs on $^{112,114}\text{Sn}$ was performed in 2023 as a proof-of-concept for measurements of statistical properties with the Oslo method at IFIN-HH [28], and to follow up a recent systematic study of the statistical properties of the Sn chain [29, 30, 31, 32, 33]. In 2024, a follow-up of the 2023 experiment was performed at the IFIN-HH to verify the consistency between data obtained from charged particle beams and γ -ray beams for the nucleus ^{128}Te for γ SFs within the context of the results from Reference [14]. While the details of this data set are still under analysis, interesting results were obtained when applying the methodology to NLDs, which will be reported

here.

2. Experiment

The experiment was conducted at the IFIN-HH 9 MV Tandem facilities in Măgurele, Romania, in the spring of 2024. The experimental setup consisted of using a combination of the ELIGANT Gamma Neutron (ELIGANT-GN) large-volume $\text{LaBr}_3\text{:Ce}$, and CeBr_3 detectors [17, 18] mounted in the mechanical frame and inside the bismuth germanate (BGO) shields of the ROSPHERE [19], a configuration that has been previously reported in detail in Reference [20]. The total angular coverage of the scintillators in this configuration was 11.95% of the solid angle. In addition to the γ -ray detectors, a charged-particle detector array consisting of silicon-strip detectors of the type Micron S7 with thicknesses of 65 μm and 1000 μm , respectively, was placed in a $\Delta E - E$ configuration in the backward direction. These detectors were placed at a distance of 28 mm from the target for the thin detector and 44 mm from the target for the thick detector, providing an angular coverage of 122° - 136° in the overlap region relative to the target.

The γ -ray detection part of the setup consisted of 20 $\text{LaBr}_3\text{:Ce}$ and CeBr_3 detectors from ELI-NP optimised for high-energy γ -rays and four high-purity germanium (HPGe) detectors for high-resolution spectroscopy of low-energy transitions to quantify background and verify the spin distributions of the excited states for different excitation energies. For calibration of the γ -ray detectors simple radioactive sources of ^{137}Cs , ^{60}Co , and ^{56}Co were used for low energies and time alignments. In the high-energy region composite sources consisting of plutonium-beryllium (PuBe) [34] inside of a sphere filled with a nickel-paraffin mixture [35] were used, providing two energy calibration points at 4.44 MeV and 9 MeV. The silicon detectors were aligned using a standard three- α source consisting of ^{239}Pu , ^{241}Am , and ^{244}Cm , as well as from elastic scattering of the protons using the in-beam data.

The target was 1.7 mg/cm^2 evaporated on a 30 $\mu\text{g}/\text{cm}^2$ backing of diamond-like carbon. The isotopic purity of the target was 98.2(2)% ^{128}Te with the largest impurity contribution from ^{130}Te (1.25%), ^{126}Te (0.37%), and ^{125}Te (0.11%) while other isotopes of Te contributed with $< 0.1\%$ each. On this target, a proton beam with an energy of 14 MeV and a typical beam current of 1.5 nA impinged, and the data were collected for 70 h. The limiting factor in these measurements was the count rate in the BGO detectors. Thus, they were disabled in the data acquisition (DAQ). The DAQ system was fully digital with the $\text{LaBr}_3\text{:Ce}$ and CeBr_3 detectors read out using CAEN V1730 digitisers running Digital Pulse Processing for Charge Integration and Pulse Shape Discrimination (DPP-PSD) firmware, and the silicon detectors as well as the HPGe detectors read out by CAEN V1725 digitisers running Digital Pulse Processing for Pulse Height Analysis (DPP-PHA) firmware.

3. Analysis

The $\text{LaBr}_3:\text{Ce}$, CeBr_3 , and silicon detectors were calibrated in energy and time-aligned using the sources described in Section 2. After calibration, the $\Delta E - E$ telescopes selected events corresponding to scattered protons. The angle of each scattered proton, θ_p , was determined from the ΔE layer, and the energy of the proton, E_p , was measured as the sum $E_p = \Delta E + E$. Given θ_p , the excitation energy of the nucleus, E_x , was calculated from the energy of an elastically scattered proton, $E_{\text{el.}}(\theta_p)$, as $E_x = E_{\text{el.}}(\theta_p) - E_p$. The γ -ray spectra from the $\text{LaBr}_3:\text{Ce}$ and CeBr_3 detectors were then extracted for each value of E_x and arranged in a two-dimensional matrix as shown in Figure 1. Some discrete peaks identified as background from ^{27}Al have

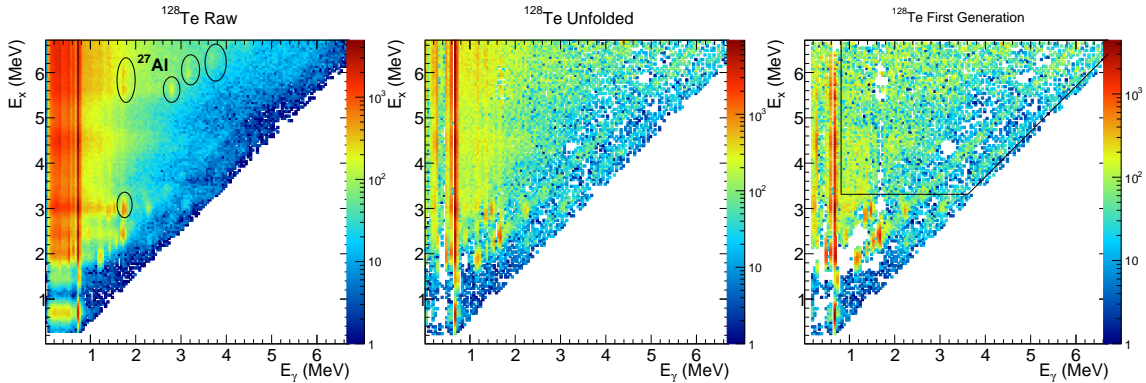


Figure 1. Raw (left), unfolded (middle) and first generation (right) matrices for ^{128}Te . The area selected for further analysis of the first-generation matrices is shown as a black outline.

been highlighted and subtracted in the unfolding step, discussed later in this text. Note that these γ -ray spectra also contain the response function of the $\text{LaBr}_3:\text{Ce}$ and CeBr_3 detectors and, as we are working in the quasi-continuum region, this response needs to be unfolded from the spectra. For this purpose, the iterative unfolding procedure [3, 36, 28] was applied using the simulated detector response from GEANT4 [37] implemented in an in-house developed software, GEANT4 and ROOT Object-Oriented Toolkit (GROOT) [38], as shown in Figure 1. As the decay probability of an excited state only depends on the NLD at the final energy, E_f of the first transition and the value of the γ SF for the energy difference $E_\gamma = E_x - E_f$, all contributions from cascading transitions were subtracted using the first-generation methodology described in detail in References [2, 4, 5], providing the so-called first generation matrix shown in Figure 1.

As we are interested in the quasi-continuum, a specific area of the matrix where the nucleus is expected to follow a statistical behaviour was selected for further analysis, shown in Figure 1 and Figure 2, and the γ -ray spectra were normalised such that each bin in the selected region would correspond to the decay probability $P(E_x, E_\gamma)$, for a γ -ray energy of E_γ from an excited state with energy E_x , as $\sum_{E_\gamma} P(E_x, E_\gamma) = 1$. Due

to the carbon backing of the target, a significant background from the first excited state in ^{12}C was present in the data. However, despite the excitation energy of this state at 4.44 MeV, due to the different reaction kinematics, the background appears at a reconstructed excitation energy of ~ 7 MeV. Thus, we have limited the high-energy range to below this background. To extract the functional forms of the NLD and the

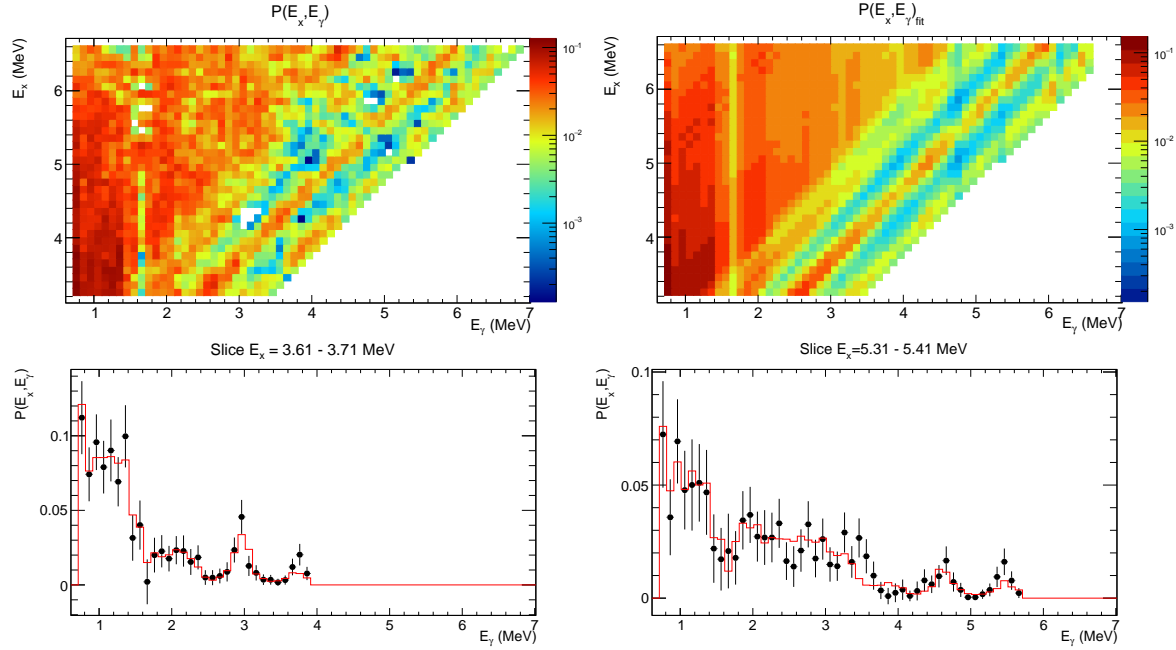


Figure 2. Experimental (top left) and best fit (top right) of the probability matrix. The bottom panels show two projections of the best fit (red line) compared with the experimental data (black circles) in the energy ranges 3.61-3.71 MeV and 5.31-5.41 MeV. The error bars include both statistical uncertainties and systematic uncertainties evaluated for the reduced $\chi^2/\text{NDF} = 1$.

γSF , a χ^2 fitting procedure was carried simultaneously over all excitation energies and γ -ray energies in the selected region [2, 3, 4, 5]

$$P(E_x, E_\gamma)_{\text{fit}} = \frac{\rho(E_x - E_\gamma)\mathcal{T}(E_\gamma)}{\sum_{E_\gamma} \rho(E_x - E_\gamma)\mathcal{T}(E_\gamma)}, \quad (1)$$

where $\rho(E_x - E_\gamma) = \rho(E_f)$ is the NLD at the final state and $\mathcal{T}(E_\gamma)$ are the transmission coefficients and they are related to the γSF , $f_{XL}(E_\gamma)$, is via the relation,

$$f_{XL}(E_\gamma) = \frac{\mathcal{T}(E_\gamma)}{2\pi E_\gamma^{2L+1}}, \quad (2)$$

where L is the multipolarity of the γ ray and we assume $L = 1$, corresponding to complete dipole domination, and X correspond to either electric (E) or magnetic (M) transitions. The result of this fit is shown in Figure 2, together with two projections at selected energies to highlight the agreement between the fit and the experimental data. At this point, we evaluate the systematic uncertainties that can originate from the data processing as well as assumptions required for the method to work, from the

reduced χ^2 by taking the number of degrees of freedom (NDF) into account such that $\chi^2/\text{NDF} = 1$. The methodological systematic uncertainties could, for example, include the validity of the Brink-Axel hypothesis that the γ SFs are independent of E_x and, thus, that a unique γ SF will fit all the data. Here, we include these uncertainties and the statistical uncertainties in the analysis. We note that around $E_\gamma \approx 1.7$ MeV, there is an oversubtraction originating from the first-generation procedure, likely originating from a small ^{27}Al background. This over-subtraction will propagate into the γ SF evaluation as an artificial dip. However, as the NLD contains the sum over all possible energies, it will not introduce any artificial features.

It is well known that the Oslo method only gives the functional form of the NLDs and γ SFs, while there are an infinite number of possible $\mathcal{T}(E_\gamma)$ and $\rho(E_x - E_\gamma)$ that can satisfy the fit in Equation (1). The relation between these possible $\mathcal{T}(E_\gamma)$ and $\rho(E_x - E_\gamma)$ is given by three parameters, A , B , and α , as [2, 3, 4, 5],

$$\tilde{\rho}(E_x - E_\gamma) = A\rho(E_x - E_\gamma) \exp[\alpha(E_x - E_\gamma)], \quad (3)$$

$$\tilde{\mathcal{T}}(E_\gamma) = B\mathcal{T}(E_\gamma) \exp(\alpha E_\gamma). \quad (4)$$

By extracting $P(E_\gamma, E_x)$ from the measured results, we have obtained one pair of solutions for $\rho(E_x)$ and $\mathcal{T}(E_\gamma)$. By normalising the $\mathcal{T}(E_\gamma)$ solution to the $(\gamma, \gamma'\gamma'')$ data [39], we can extract the parameters B , corresponding to the absolute values, and α , corresponding to the slope, from equation (4), shown in Figure 3. With the slope known, we can fix the absolute value of the nuclear level densities, parameter A , from the complete spectroscopy of known states in the energy range 2-3 MeV, also shown in Figure 3 and listed in Table 1, under the assumption that the γ SF from the $(\gamma, \gamma'\gamma'')$ data, mainly populating a very sharp spin (J) and parity (P) distribution with $J^P \approx 1^\pm$, is close enough to the γ SF from higher spin states populated in inelastic (p, p' γ) scattering.

4. Discussion

The overall agreement between the shape of the γ SF from the $(\gamma, \gamma'\gamma'')$ data [39] is shown in Figure 3. Note that since the $(\gamma, \gamma'\gamma'')$ data were used for normalisation of the absolute magnitude and the total slope of the γ SF, only the relative shapes can be used to evaluate the consistency. For comparison, we also include the following microscopic calculations and parametrisations of the γ SFs as implemented in the TALYS [41, 42] code: the temperature-dependent Hartree-Fock-Bogolyubov (HFB) by Goriely [43], the HFB and Quasiparticle Random Phase Approximation (QRPA) calculations with the Gogny D1M interaction [44], and the simplified version of the modified Lorentzian (SMLO) function from the recommendations of the International Atomic Energy Agency (IAEA) Coordinated Research Project (CRP) on γ SFs [45, 46].

On the NLD side, the procedure described in Section 3 should provide us with the NLD directly from experimental data, without the need to invoke model-dependent extrapolations to the neutron separation energy, typically via the constant temperature

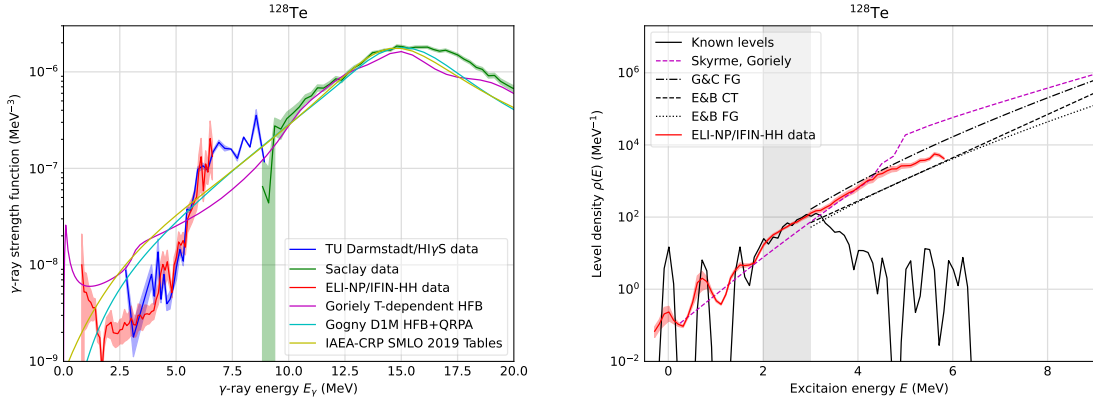


Figure 3. (Left) Experimental γ -ray strength functions of ^{128}Te obtained from this work (ELI-NP/IFIN-HH), $(\gamma, \gamma', \gamma'')$ data from Reference [39] (TU Darmstadt/HI γ S), and (γ, n) cross-section data from Reference [40] (Saclay). For comparison, three typical parametrisations, as implemented in the TALYS code, are shown as solid lines for electric dipole strength and dashed lines for magnetic dipole strength. (Right) Nuclear level density of ^{128}Te . The shaded region shows the range for fitting to known spectroscopic states. The transparent bands correspond to the statistical and systematic uncertainties. Three phenomenological parametrisations discussed in the text and one microscopic model implemented in TALYS are shown for comparison.

Table 1. Experimental results on the nuclear level density (NLD) in ^{128}Te .

Energy (MeV)	NLD (MeV^{-1})	Energy (MeV)	NLD ($\times 10 \text{ MeV}^{-1}$)	Energy (MeV)	NLD ($\times 10^2 \text{ MeV}^{-1}$)	Energy (MeV)	NLD ($\times 10^3 \text{ MeV}^{-1}$)
-0.2875	0.069(22)	1.3125	0.204(24)	2.9125	1.043(10)	4.5125	1.61(28)
-0.1875	0.11(4)	1.4125	0.336(4)	3.0125	1.30(14)	4.6125	1.91(34)
-0.0875	0.21(11)	1.5125	0.471(7)	3.1125	1.49(16)	4.7125	2.16(4)
0.0125	0.24(10)	1.6125	0.454(5)	3.2125	1.53(16)	4.8125	2.17(31)
0.1125	0.138(27)	1.7125	0.471(4)	3.3125	1.83(20)	4.9125	2.62(4)
0.2125	0.106(13)	1.8125	0.535(4)	3.4125	2.12(25)	5.0125	2.64(34)
0.3125	0.0941(8)	1.9125	0.98(8)	3.5125	2.74(4)	5.1125	2.68(30)
0.4125	0.18(20)	2.0125	1.72(15)	3.6125	3.33(5)	5.2125	3.07(33)
0.5125	0.43(9)	2.1125	2.42(19)	3.7125	3.99(6)	5.3125	3.69(4)
0.6125	1.52(8)	2.2125	3.22(22)	3.8125	4.75(8)	5.4125	3.75(35)
0.7125	2.0(11)	2.3125	3.80(25)	3.9125	5.36(8)	5.5125	4.15(4)
0.8125	1.63(6)	2.4125	4.65(25)	4.0125	6.7(11)	5.6125	5.62(5)
0.9125	0.84(13)	2.5125	5.45(29)	4.1125	8.3(14)	5.7125	5.22(5)
1.0125	0.48(4)	2.6125	6.63(4)	4.2125	10.4(19)	5.8125	4.21(29)
1.1125	0.381(20)	2.7125	7.31(6)	4.3125	10.9(18)		
1.2125	0.713(5)	2.8125	8.85(7)	4.4125	15.1(30)		

or the Fermi gas model. Thus, comparing the experimental data presented here to these two common extrapolations would be interesting. The two models are simple phenomenological two-parameter models that are based on the observation of empirical

nuclear properties. Here, we will use the formulation of these models presented in Reference [47].

The constant temperature model [48] is based on the observation that the number of nuclear levels typically increases with a simple exponential behaviour with increasing excitation energy, implying the nucleus stays at a constant temperature, T , in the applicable energy range. This description is justified by the increased breaking of Cooper pairs with increasing excitation energy, keeping the mean energy per nucleon constant. Thus, the NLD as a function of E_x and J , in the constant temperature approximation, $\rho_{\text{CT}}(E_x, J)$, can be expressed as

$$\rho_{\text{CT}}(E_x, J) = f(J) \frac{1}{T} \exp\left(\frac{E_x - E_0}{T}\right). \quad (5)$$

In addition to T , a back-shift parameter, E_0 , has been introduced to adjust for the finite energy where the statistical properties dominate.

The Fermi gas NLD [47], $\rho_{\text{FG}}(E_x, J)$, on the other hand, is justified considering the nucleus as a gas of non-interacting fermions within the nuclear volume and calculated the number of possibilities to distribute the excitation energy on these [49], considering single-particle states,

$$\rho_{\text{FG}}(E_x, J) = f(J) \frac{\exp[2a(E_x - E_1)]}{12\sqrt{2}\sigma a^{1/4}(E_x - E_1)^{5/4}}. \quad (6)$$

This expression also consists of two main parameters, the level density parameter a and the Fermi back-shift parameter E_1 . In addition, the spin cut-off parameter, σ , is included explicitly in the expression (6). In fact, in both equations (5) and (6), the spin distribution has been considered independent from E_x and separated into the function $f(J)$,

$$f(J) = \frac{2J + 1}{2\sigma^2} \exp\left[-\frac{(J + 1/2)^2}{2\sigma^2}\right]. \quad (7)$$

Note that this energy independence of $f(J)$ is an approximation, and in an actual nucleus, there indeed is a likely energy dependence of σ and, therefore, also on $f(J)$.

To compare the experimental data with the phenomenological descriptions in equations (5-7), we employed a selection of typical parametrisations of the data from Gilbert and Cameron [48], and von Egidy and Bucurescu [50]. The extraction of parameters for equations (5-7) was performed using the ROBIN code version 1.92 [51]. The obtained parameters are listed in Table 2 and the corresponding NLDs are shown in Figure 3. In addition to the phenomenological models, the calculated results from the Reference Input Parameter Library (RIPL) calculated from the Skyrme force, as implemented in TALYS 1.95, are also shown [52].

5. Conclusion and outlook

We have extracted the nuclear level density of ^{128}Te from a $(p, p'\gamma)$ scattering experiment using the large-volume $\text{LaBr}_3:\text{Ce}$ and CeBr_3 detectors from ELI-NP at the 9 MV tandem

Table 2. Parameters for different parametrisations of the constant temperature (CT) and Fermi gas (FG) models by Gilbert and Cameron (G&C) and von Egidy and Bucurescu (E&B). The level density parameter is denoted a , the Fermi back-shift E_1 , the nuclear temperature T , and the constant temperature back-shift E_0 . We also list the calculated temperature $T(S_n)$, nuclear level density $\rho(S_n)$, and spin cut-off $\sigma(S_n)$, at the neutron threshold S_n .

Model	a MeV $^{-1}$	E_1 MeV	T MeV	E_0 MeV	$T(S_n)$ MeV	$\rho(S_n)$ MeV $^{-1}$	$\sigma(S_n)$
G&C (FG) [48]	13.073	0.680			0.78723	0.40912×10^6	4.818
E&B (CT) [50]			0.724	0.159	0.724	0.20476×10^6	4.002
E&B (FG) [50]	11.738	0.782			0.82556	0.14×10^6	4.414

facilities at IFIN-HH. The decay data were normalised using photonuclear data, which provides nuclear level densities without intrinsic model dependencies from the constant temperature or Fermi gas models. The nuclear level density follows closely between the expectations from these two models, but we observe a clear divergence from the microscopic model based on the Skyrme force. Further work will include the in-depth study of the γ -ray strength functions from this data, in particular, to investigate how assumptions like the validity of the Brink-Axel hypothesis and the contribution from the spin distribution affect γ -ray strength-function results in both photonuclear data and charged particle data.

Acknowledgements

PAS, AK, RB, MB, CCo, NMF, AGa, RL, CMi, AS, DAT, AT, GVT, and SU were supported by the ELI-RO program funded by the Institute of Atomic Physics, Măgurele, Romania, contract number ELI-RO/RDI/2024-002 (CIPHERS) and SA, DLB, SRB, RC, and TP ELI-RO/RDI/2024-007 (ELITE). The remaining authors from ELI-NP acknowledge the support of the Romanian Ministry of Research and Innovation under research contract PN 23 21 01 06. This project has received funding from the European Union's Horizon Europe Research and Innovation programme under Grant Agreement No 101057511 (EURO-LABS).

References

- [1] Wiedeking M and Goriely S 2024 *Phil. Trans. R. Soc. A* **382** 20230125
- [2] Guttormsen M, Ramsøy T and Rekestad J 1987 *Nucl. Instrum. Methods Phys. Res. A* **255** 518
- [3] Guttormsen M, Tveter T S, Bergholt L, Ingebretsen F and Rekestad J 1996 *Nucl. Instrum. Methods Phys. Res. A* **374** 371
- [4] Schiller A, Bergholt L, Guttormsen M, Melby E, Rekestad J and Siem S 2000 *Nucl. Instrum. Methods Phys. Res. A* **447** 498
- [5] Larsen A C *et al* 2011 *Phys. Rev. C* **83** 034315
- [6] Voinov A V *et al* 2019 *Phys. Rev. C* **99** 054609
- [7] Roy P *et al* 2021 *Eur. Phys. J. A* **57** 48

- [8] Usman I *et al* 2011 *Phys. Rev. C* **84** 054322
- [9] Filipescu D *et al* 2015 *Eur. Phys. J.* **A51** 185
- [10] Gales S, Balabanski D L, Negoita F, Tesileanu O, Ur C A, Ursescu D and Zamfir N V 2016 *Phys. Scr.* **91** 093004
- [11] Gales S *et al* 2018 *Rep. Prog. Phys.* **81** 094301
- [12] Tanaka K A *et al* 2020 *Matter Radiat. Extremes* **5** 024402
- [13] Constantin P, Matei C and Ur C A 2024 *Phys. Rev. Accel. Beams* **27** 021601
- [14] Isaak J *et al* 2019 *Phys. Lett. B* **788** 225
- [15] Brink D M 1955 *Some aspects of the interaction of fields with matter* Ph.D. thesis University of Oxford Oxford, United Kingdom
- [16] Axel P 1962 *Phys. Rev.* **126** 671
- [17] Camera F *et al* 2016 *Rom. Rep. Phys.* **68** S539
- [18] Söderström P A *et al* 2022 *Nucl. Instrum. Methods Phys. Res. A* **1027** 166171
- [19] Bucurescu D *et al* 2016 *Nucl. Instrum. Methods Phys. Res. A* **837** 1
- [20] Aogaki S *et al* 2023 *Nucl. Instrum. Methods Phys. Res. A* **1056** 168628
- [21] Kuşoğlu A *et al* 2024 *Nuovo Cimento C* **47** 47
- [22] Kuşoğlu A *et al* 2024 *Phys. Rev. Lett.* **133**(7) 072502
- [23] Kuşoğlu A *et al* 2024 *EPJ Web Conf.* **311** 00020
- [24] Kuşoğlu A 2024 *Sci. Bull.* **69** 3303
- [25] Wieland O *et al* 2024 *Nuovo Cimento C* **47** 24
- [26] Söderström P A *et al* 2024 *Nuovo Cimento C* **47** 58
- [27] Sakanashi K *et al* 2024 *EPJ Web Conf* **306** 01047
- [28] Söderström P A *et al* 2024 Statistical properties and photon strength functions of the $^{112,114}\text{Sn}$ isotopes below the neutron separation threshold In manuscript. [arXiv:2410.06907](https://arxiv.org/abs/2410.06907)
- [29] Markova M *et al* 2021 *Phys. Rev. Lett.* **127** 182501
- [30] Markova M *et al* 2022 *Phys. Rev. C* **106** 034322
- [31] Markova M *et al* 2023 *Phys. Rev. C* **108** 014315
- [32] Markova M *et al* 2024 *Phys. Rev. C* **109** 054311
- [33] Markova M, von Neumann-Cosel P and Litvinova E 2025 *Phys. Lett. B* **860** 139216
- [34] Söderström P A, Matei C, Capponi L, Açıksöz E, Balabanski D L and Mitu I O 2021 *Appl. Radiat. Isot.* **167** 109441
- [35] Söderström P A *et al* 2023 *Appl. Radiat. Isot.* **191** 110559
- [36] Söderström P A *et al* 2019 *J. Instrum.* **14** T11007
- [37] Agostinelli S *et al* 2003 *Nucl. Instrum. Methods Phys. Res. A* **506** 250
- [38] Lattuada D *et al* 2017 *EPJ Web Conf.* **165** 01034
- [39] Isaak J *et al* 2021 *Phys. Rev. C* **103** 044317
- [40] Leprêtre A, Beil H, Bergère R, Carlos P, Fagot J, Miniac A D, Veyssiére A and Miyase H 1976 *Nucl. Phys. A* **258** 350
- [41] Koning A J, Hilaire S and Duijvestijn M C 2008 TALYS-1.0 *Proceedings of the International Conference on Nuclear Data for Science and Technology* vol 211 ed Bersillon O, Günsing F, Bauge E, Jacqmin R and Leray S (EDP Sciences) p 058
- [42] Koning A J and Rochman D 2012 *Nucl. Data Sheets* **113** 2841
- [43] Hilaire S, Girod M, Goriely S and Koning A J 2012 *Phys. Rev. C* **86** 064317
- [44] Goriely S, Hilaire S, Péru S and Sieja K 2018 *Phys. Rev. C* **98** 014327
- [45] Kawano T *et al* 2020 *Nucl. Data Sheets* **163** 109
- [46] Goriely S *et al* 2019 *Eur. Phys. J. A* **55** 172
- [47] von Egidy T, Schmidt H H and Behkams A N 1988 *Nucl. Phys. A* **481** 189
- [48] Gilbert A and Cameron A G W 1965 *Can. J. Phys.* **43** 1446
- [49] Bethe H A 1936 *Phys. Rev.* **50** 332
- [50] von Egidy T and Bucurescu D 2009 *Phys. Rev. C* **80** 054310
- [51] Guttormsen M 2022 ROBIN, in OsloSoftware <https://github.com/oslocyclotronlab/>

`oslo-method-software`, DOI: 10.5281/zenodo.6024876

[52] Goriely S, Tondeur F and Pearson J M 2001 *Atom. Data Nucl. Data Tables* **77** 311